Weaver: Hexapod Robot for Autonomous Navigation on Unstructured Terrain

Marko Bjelonic[*]
Robotic Systems Lab
ETH Zürich, 8092 Zürich
Switzerland

Navinda Kottege[†]
Robotics and Autonomous Systems Group
CSIRO, Pullenvale, QLD 4069
Australia

Timon Homberger[*]
Department of Mechanical and Process Engineering
ETH Zürich, 8092 Zürich
Switzerland

Paulo Borges
Robotics and Autonomous Systems Group
CSIRO, Pullenvale, QLD 4069
Australia

Philipp Beckerle
Institute for Mechatronic Systems in Mechanical Engineering
Technische Universität Darmstadt, 64287 Darmstadt
Germany

Margarita Chli
Vision for Robotics Lab
ETH Zürich, 8092 Zürich
Switzerland

Abstract

Legged robots are an efficient alternative for navigation in challenging terrain. In this paper we describe Weaver, a six legged robot that is designed to perform autonomous navigation in unstructured terrain. It uses stereo vision and proprioceptive sensing based terrain perception for adaptive control while using visual-inertial odometry for autonomous waypoint based navigation. Terrain perception generates a minimal representation of the traversed environment in terms of roughness and step height. This reduces the complexity of the terrain model significantly, enabling the robot to feed back information about the environment into its controller. Furthermore, we combine exteroceptive and proprioceptive sensing to enhance the terrain perception capabilities, especially in situations where the stereo camera is not able to generate an accurate representation of the environment. The adaptation approach described also exploits the unique properties of legged robots by adapting the virtual stiffness, stride frequency and stride height. Weaver's unique leg design with five joints per leg improves locomotion on high gradient slopes and this novel configuration is further analyzed. Using these approaches, we present an experimental evaluation of this fully self-contained hexapod performing autonomous navigation on a multi-terrain testbed and in outdoor terrain.

1   Introduction

Legged robots have unique properties that allow them to potentially outperform wheeled platforms in challenging and rough terrain. This advantage stems from the increased mobility and versatility compared to

---

[*]M. Bjelonic and T. Homberger were with the Robotics and Autonomous Systems Group, CSIRO, Pullenvale, QLD 4069, Australia at the time of this work.

[†]All correspondence should be addressed to N. Kottege at `navinda.kottege@csiro.au`.

Figure 1: Hexapod robot Weaver on (a) the multi-terrain testbed and (b) outdoor terrain.

tracked robots. Yet, the high mobility comes at the cost of high motion complexity, making the building and control of such systems still challenging. A high degree of mobility and autonomy is required especially for systems designed for field missions in the real world. The legged robots Lauron V (Roennau et al., 2014a), ANYmal (Hutter et al., 2016), HyQ2Max (Semini et al., 2017) and MAX (Elfes et al., 2017) are some recent examples of ongoing efforts in this topic.

We introduce a novel paradigm for legged robots, re-conceptualizing Weaver, a high degree-of-freedom hexapod robot with proprioceptive control and exteroceptive terrain perception capabilities using stereo vision. Previous work showed vision-based exteroceptive terrain perception to adapt the robot's locomotion parameters (Bjelonic et al., 2017, 2016, Homberger et al., 2016). The goal of this work is to extend our previous control and terrain perception framework to make the robot more robust in outdoor terrain. Our contribution is threefold. First, we introduce a proprioceptive terrain perception framework using the state feedback of the robot, i.e., motor readings and free-floating base motion, and a thorough analysis of this terrain perception method is presented. Second, we combine proprioceptive and exteroceptive sensing to adapt the robot's control parameters. This method allows for autonomous navigation in challenging outdoor terrain with improved energy efficiency in locomotion while being robust against sensor errors. Finally, we show a high verity of experimental results in indoor and outdoor environments.

Both terrain perception methods produce a minimal representation of the environment. A set of control parameters is generated that is optimal with respect to the terrain representation. This parameter set exploits three unique properties of legged locomotion by controlling the *virtual stiffness* of the impedance controller, *stride frequency* and *stride height*. Combining both exteroceptive and proprioceptive sources of information enhances the overall terrain perception significantly. For example, stereo vision by itself may lead to incorrect estimations in conditions such as walking in high grass, bad illumination, motion blur, or dynamic scenes. The proposed combination of the two modalities provides robustness in these situations by switching to proprioceptive terrain perception to maintain energy efficient locomotion. In addition, autonomous navigation is achieved by applying a path following algorithm based on state estimation using visual-inertial odometry. Comprehensive experiments for evaluating performance of the proposed methods are performed on a multi-terrain testbed as well as on outdoor terrain. The results illustrate the applicability of the system.

The rest of this paper is organized as follows: The problem of locomotion in unknown and challenging environments along with proposed solutions are discussed in Section 2. Weaver's hardware setup and novel leg configuration with five degrees of freedom (DoF) is analyzed in Section 3. Section 4 introduces the overall control architecture of Weaver. In particular, Sections 4.3.2 and 4.3.3 contain the technical description of the main novel contributions of this work. In Section 5 the experimental setup is described, with results shown in Section 6 and thoroughly analyzed in Section 7. Section 8 concludes the paper with insights for extensions.

2 Locomotion in Challenging Terrain

A benchmark problem in legged robotics is locomotion in unknown and challenging terrain. In this paper, we focus on algorithms that enable legged robots to traverse these kinds of terrain. A common approach is to use some type of sensing to generate a representation of the environment, which is used to navigate the robot through the terrain.

Wermelinger et al. (2016) builds a traversability map based on slope, roughness, and steps of the terrain. The terrain estimation is based on an elevation map, which is built using rotating laser sensors. A sampling-based planner uses the RRT^* algorithm to optimize the path length and safety based on the generated traversability map. Similarly, the quadruped robot BigDog generates a costmap using laser scanning and stereo vision (Wooden et al., 2010). This is used for path planning in unstructured forest environments. Traversability estimation and path planning based on the $D^* Lite$ algorithm has also been exploited (Chilian and Hirschmüller, 2009). The weakness of these approaches is that the path planner avoids rough terrain by navigating the robot through even terrain that could also be potentially traversed by a wheeled robot. Therefore, these approaches are not fully exploiting the unique properties of legged robots in rough terrain. In contrast, Kolter et al. (2008) propose an approach that is able to navigate the quadrupedal robot LittleDog through rough terrain by estimating exactly the terrain and the state of the robot. They use exact path planning of each foot to solve the rough terrain problem with an a priori 3D model of the environment and motion capture markers for state estimation. However, trajectory planning of the feet without reactive stabilization is insufficient for practical walking robots due to unpredictable and dynamic disturbances, such as bumps and slippage (Wettergreen et al., 1995). In addition, exact path planning of the feet often requires an accurate map of the environment and accurate localization inside the map as in the case of Kolter et al. (2008), which are not always available when operating in outdoor terrain. Stejskal et al. (2016) use proprioceptive terrain perception approaches for autonomous navigation. In their work the robot is able to follow a road blindly and the only feedback considered is an estimation of tactile information that is determined from the robot's motors. This approach limits the application to road like environments with a clear transition between two different kinds of terrains.

A large body of literature already addresses path planning in unstructured terrain using an environmental map. Instead, we go a step further by tightly coupling the representation of the environment with the control architecture. We generate a roughness and a step height of the terrain using exteroceptive and proprioceptive sensing based on several terrain features. In contrast to the work that uses this terrain information for path planning, this is further used to adapt the control algorithm of the legged system. Control adaptation for legged robots was already proposed by Hodgins and Raibert (1991). They investigate controlling step length in the context of a dynamic biped robot that actively balances itself as it runs. However, the authors only show three methods to adjust the step length but they do not provide further insights on how this parameter should change in varying terrain. In contrast, Fukuoka et al. (2003) adapt the gains of a PD controller at the joint based on several proprioceptive feedback signals. Arena et al. (2005) combine both proprioceptive and exteroceptive information to change the posture of the robot. Albeit it is verified only in simulation, the robot is able to climb obstacles by using the combined information. Similar to our approach, Pecka et al. (2017) show a tracked platform that is able to compensate incomplete laser sensor measurements with a robotic arm, e.g., below water surfaces. However, the approach is only used to compensate for incomplete sensor measurements. To the best of our knowledge, our work is the first to combine exteroceptive and proprioceptive terrain characterization for adaptive control of a real legged robot. In addition, our approach does not require an exact estimation of the terrain and the robot due to the reactive control methodology. Thus, exact path planning of each foot position is not necessary.

Our second novelty is the combination of exteroceptive and proprioceptive sensing to enhance the terrain estimation in situations where exteroceptive sensing fails (e.g., high grass, bad illumination, motion blur and dynamic scenes). Terrain estimation using feedback from proprioceptive sensing is one of the major contributions of our work. The hexapod robot LAURON V (Roennau et al., 2014b) calculates the inclination angle of the terrain by incorporating inertial and joint position signals. Forward kinematics yields the Cartesian

position of the feet and by fitting a plane equation into the foot positions using a least squares estimation the inclination of the ground can be calculated. Similarly, the quadruped robot StarlETH (Gehring et al., 2015) fuses measurements from an Inertial Measurement Unit (IMU), kinematic data from joint encoders and contact information from force sensors to estimate the local inclination of the terrain. The fusion of these three types of sensors is even robust for dynamic trotting, as only two support legs are available for solving the least-squares problem, which implies that at least three measurements are available. Since the estimated position of the robot drifts over time, the feet positions drift as well. The work in (Hoepflinger et al., 2013) uses unsupervised identification and prediction of foothold robustness. Moreover, the robustness is defined by a function of the achievable ground reaction forces. To this end, the robots leg is employed to haptically explore an unknown foothold. We extend the related work by generating not only the inclination angle of the terrain but also the roughness and step height from a set of six terrain features. For this purpose, Weaver incorporates the signals from an IMU, joint position encoders and joint current sensors. This is further combined with the exteroceptive perception to enhance the locomotion in varying terrain.

3   Hexapod Robot Weaver

Weaver is fully self-contained in terms of processing and energy. Figure 2 gives an overview of the main hardware components on-board the robot. Table 1 contains the main hardware specifications for Weaver. Based on the current hardware configuration, the robot has a run-time of approximately 1 hr. The following subsections give more details about the hardware on the robot and its novel kinematic leg design.
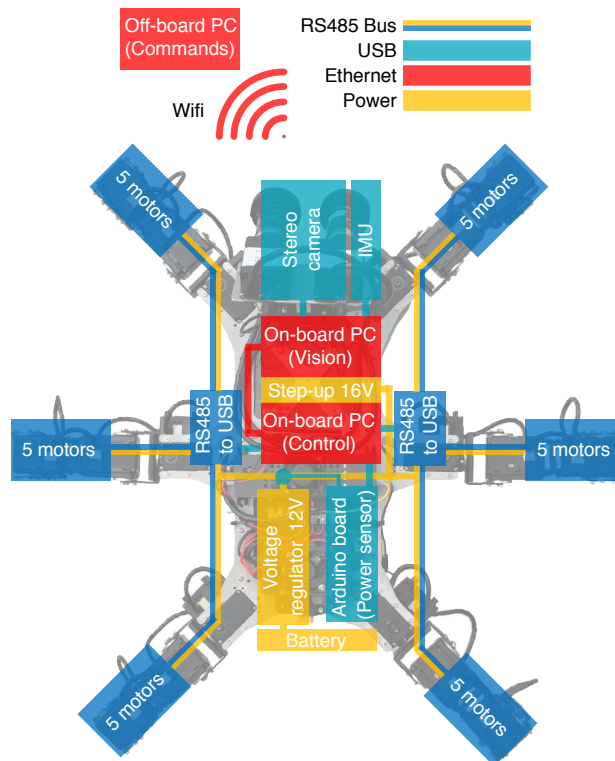

Figure 2: Main hardware components of Weaver and their connectivity.

Table 1: Hardware specifications of Weaver Bjelonic et al. (2017).

Type	Description
Mass	9.3 kg (without battery), 10.3 kg (with battery)
Dimensions (standing)	Width: 0.63 m, Length: 0.62 m, Height (ground clearance): 0.2 m
Servomotors	Dynamixel MX-64 (Coxa, Tibia and Tarsus joints) and Dynamixel MX-106 ($Coxa_t$ and Femur joints)
Power supply	7-cell LiPo battery (25.9 V, 5000 mAh)
On-board PC	2× Intel NUC mini PC (Intel Core i7 processor, 16 GB RAM) running Robot Operation System (ROS) in an Ubuntu environment
Sensors	IMU (Microstrain GX3 - 100 Hz) and 2× Cameras (Pointgrey Grasshopper3), on-board voltage and current sensors (20 Hz)

3.1 Actuation, Processing and Sensing

The actuation of the 30 joints is based on a closed-loop servomechanism. The motor controllers precisely track the desired and current angular positions by using a PID control loop. Each joint is controlled as a single-input single-output system (SISO) and coupling effects are treated as disturbances. The main objectives of the independent joint controller are trajectory tracking and disturbance rejection. As discussed in Section 4.2.2, the impedance controller depends on the torque acting on each of the joints. The torque from the servomotors is estimated by using the corresponding current signals. The torque M is modeled as a linear function of the current i, i.e., $M = k_C \cdot i$. This estimation neglects large friction losses and other nonlinear effects in the servomotors. The constant calibration gain k_C is determined in an experiment with an ATI Mini45 Force/Torque sensor. All motors are connected to the control PC by two separate buses with a total update rate of 50 Hz.

All computation is processed on-board and online. Two Intel NUC PCs are connected over an internal Gigabit ethernet network. A human operator is able to access the on-board PCs and specify desired waypoints for the robot to reach via an off-board PC (connected via Wifi). Both on-board PCs share the computational load of the algorithms introduced earlier. Moreover, the processing is divided into vision processing (including visual inertial odometry) and legged robot control. The nominal CPU utilization is 81% on the vision PC and 20% on the control PC. The signals are distributed over the network by the Robot Operating System (ROS) running on Ubuntu 14.04 LTS. The ROS master handles the communication between the different PCs.

Section 4.1.1 discusses OKVIS, an algorithm that relies on camera and IMU readings to perform visual-inertial odometry. On Weaver, a custom built stereo camera mount holds two PG Grasshopper3 cameras with a resolution of 1920 x 1440 and a Microstrain 3DM-GX3-25 IMU. The pitch angle of the mount is customized with a lockable revolute joint to let the stereo pair capture a desired terrain patch upfront the robots walking direction. For spatial calibration of this setup the KALIBR calibration package with an Aprilgrid is used (Furgale et al., 2013). The camera triggering is synchronized via a GPIO cable. OKVIS was originally designed for the fully time-synchronized and factory-calibrated VI-sensor (Nikolic et al., 2014). In contrast to reported experiments, where the sensor unit is either hand held or mounted on a car (Leutenegger et al., 2013), in this work the camera pair is tilted towards the ground (since the terrain perception requires the terrain area in front of the robot). This leads to a field of view limited to objects relatively close to the cameras and thus a limited number of detectable features in the image streams. When maneuvering on uneven terrain, motion tends to be bumpy which further influences the performance of the algorithm.

The on-board voltage and current sensors are used to calculate the electrical power consumption P of the robot at 20 Hz. This information is used to calculate the energetic cost of transport.

3.2 Over-actuated Leg Design

Weaver's configuration consists of five DoF per leg, such that the robot has 30 DoF in total. Figure 3 illustrates the naming convention of all joints, links and frames. The navigation system takes into account the robot's body frame $(o_1 x_1 y_1 z_1)$ relative to a fixed world frame $(o_0 x_0 y_0 z_0)$. Kinematics of the leg is derived relative to the leg frame (or Coxa frame) $(o_2 x_2 y_2 z_2)$. This over-actuated design of the leg is used to improve locomotion on inclined terrain by adapting the orientation of the feet.

The Jacobian matrix for one leg $\mathbf{J_e} \in \mathbb{R}^{6 \times 5}$ maps the joint velocity vector $\dot{\mathbf{q}} \in \mathbb{R}^5$ into the Cartesian twist of the foot tip. Cartesian twist of the foot tip is represented by the linear velocity vector $\mathbf{v_e} \in \mathbb{R}^3$ and angular velocity vector $\boldsymbol{\omega_e} \in \mathbb{R}^3$ relative to the leg frame $(o_2 x_2 y_2 z_2)$. Similarly, the Jacobian is used to map joint torques $\boldsymbol{\tau} \in \mathbb{R}^5$ into the Cartesian wrench at the foot tip given by the linear force vector $\mathbf{f_e} \in \mathbb{R}^3$ and the torque vector $\mathbf{m_e} \in \mathbb{R}^3$ with respect to the leg frame $(o_2 x_2 y_2 z_2)$. The static wrench transmission yields

$$\begin{bmatrix} \mathbf{f_e} \\ \boldsymbol{m_e} \end{bmatrix} = (\mathbf{J_e}(\mathbf{q})^T)^{-1} \cdot \boldsymbol{\tau} \tag{1}$$

Starting from a certain configuration the robot should be able to move its foot tip equally well in every direction. For this purpose, Yoshikawa (1985) described how to analyze the manipulability of robotic manipulators. Manipulability defines the ability to change position of the foot tip given a specific joint configuration. Similar to the analysis by Görner et al. (2008), the following paragraph discusses the manipulability of the foot tip for different joint configurations.

The Jacobian $\mathbf{J_e}$ scales the input $\dot{\mathbf{q}}$ to produce the output $\mathbf{v_e}$. In other words, the Jacobian maps the unit sphere of angular velocities in joint space onto a velocity ellipsoid of the foot tip in Cartesian space. This can also be shown by replacing the Jacobian by its Singular Value Decomposition (SVD). The singular values or respectively the length of the principal axes of the ellipsoid are given by $\sigma_1(q)$, $\sigma_2(q)$ and $\sigma_3(q)$. Furthermore, the robot is able to generate the best Cartesian velocity in the direction of the axis corresponding to the largest singular value. The volume of the ellipsoid is a measure for the manipulability (i.e., velocity generation capacity) and it is given by the following expression Görner et al. (2008):

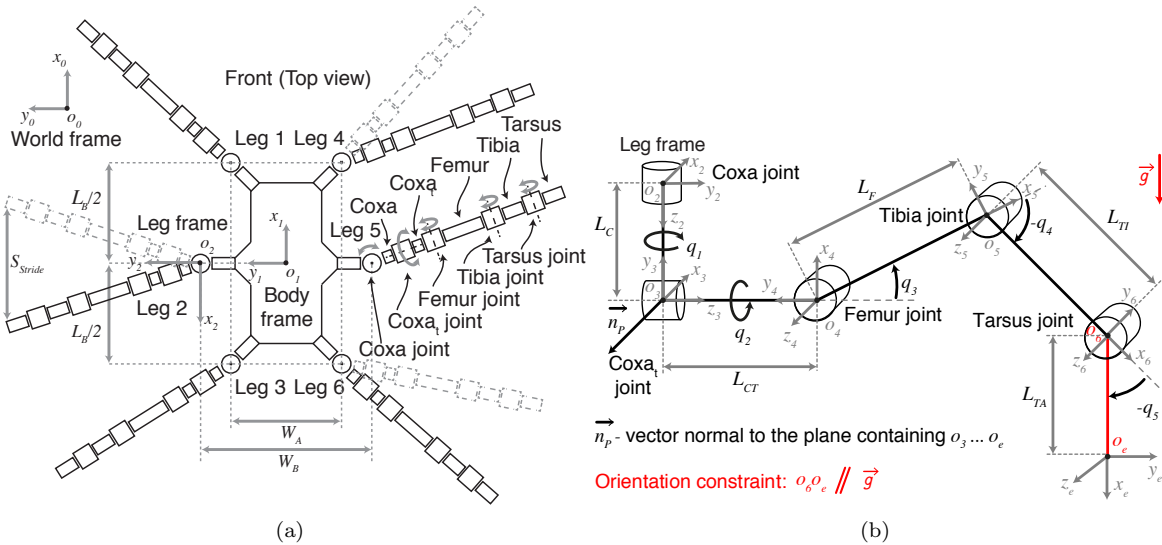$$V(q) = \frac{4}{3}\pi\sigma_1(q)\sigma_2(q)\sigma_3(q) \tag{2}$$

Figure 3: Structure, dimensions and frames of Weaver's body (a) and of the five DoF leg (b).

The equivalent force ellipsoid is dual to the velocity ellipsoid since the transmission from joint torques to forces at the foot tip in Cartesian space in (1) is defined by the inverse of the Jacobian transpose. This means, that the best direction to generate forces coincides with the worst direction to generate velocities (Görner et al., 2008). Aligning this direction with the gravitational vector, reduces the torque in each motor because the gravitational force is supported with least amount of effort. On inclined terrain the leg orientation needs to adapt in order to align the gravitational force with the highest singular value direction, i.e., highest length of the principle axis of the force ellipsoid σ_i.

Weaver's novel leg configuration features five DoF. Many of the previously presented hexapod robots are able to control the Cartesian *position* of the foot tip only Bjelonic et al. (2016). With Weaver's five DoF configuration, trying to solve inverse kinematics results in ambiguities. Therefore, the foot tip is also constrained by a desired *orientation* (see Figure 3). Based on the analysis of the force ellipsoid, inverse kinematics is designed to align the force ellipsoid of the foot tip with the gravity vector. The orientation of the gravity vector with respect to the leg frame $(o_2 x_2 y_2 z_2)$ is defined by two control angles δ_d and β_d. Both angles are specified by the inclination controller that is discussed in Section 4.2.3. The design of the inverse kinematics is inspired by Roennau et al. (2014a) and a complete solution for every joint angle can be found in Bjelonic et al. (2016).

4   Hybrid Controller

Weaver's novel control paradigm incorporates *proactive* and *reactive* control into one *hybrid control* architecture. An overview of the control elements is given in Figure 4. The adaptation controller combines exteroceptive and proprioceptive sensing to enhance locomotion on varying and rough terrain structures. The parameters of the stride trajectory generator and the virtual stiffness of the impedance controller are set based on this terrain estimation. In addition, the inclination controller improves the locomotion on high gradient slopes by specifying a desired body pose and a desired foot tip orientation. The navigation system simultaneously gets the position of the robot via visual-inertial odometry and sets the desired velocity of the robot's body using a path following algorithm, all of which are implemented on-board the robot. The main contribution of our work stems from a novel proprioceptive terrain perception method and extensions of the vision-based controller adaptation framework (Bjelonic et al., 2017). The following subsections present the different control elements in more detail.

4.1   Navigation System

The navigation system focuses on a high-level abstraction of the robot's path without relying on detailed maps of the environment. This means that the robot is only using its position and a desired path for navigation. Based on waypoints set by the user or a path planner, the navigation system generates high level velocity commands (i.e., angular and linear velocities for the body) assuming flat terrain. During autonomous maneuvering, the stride trajectory generator, impedance controller, adaptation controller and inclination controller command the legs' position and orientation in order to negotiate non-flat varying terrain types.

4.1.1   Visual-Inertial Odometry

The position and orientation of the robot's body $(o_0 x_1 y_1 z_1)$ with respect to the world frame $(o_0 x_0 y_0 z_0)$ in Figure 3 are obtained through visual-inertial odometry. For this purpose, an open-source keyframe based visual-inertial odometry algorithm (OKVIS) is used Bjelonic et al. (2017), Leutenegger et al. (2013, 2014). This tightly fuses stereo camera and IMU readings using nonlinear optimization. The real-time operation is achieved by applying keyframes that partially marginalize old states to maintain a bounded-sized optimization window.
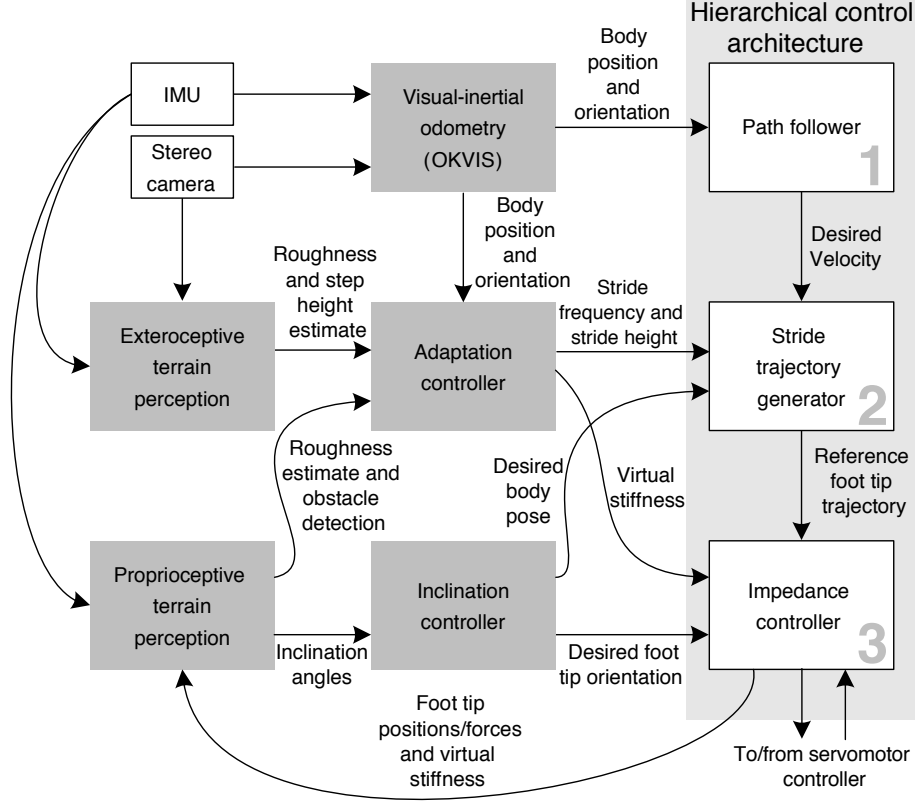
Figure 4: Hybrid controller of Weaver.

4.1.2 Path Follower

The path follower uses a lookahead-based steering law for straight line segments between waypoints (Bjelonic et al., 2017, Breivik and Fossen, 2009). It takes into account the robot's position o_1 and orientation q_{yaw} with respect to the world frame $(o_0 x_0 y_0 z_0)$. As can be seen in Figure 5, the path following algorithm produces a desired forward V_x, sideways V_y and rotational motion $\dot{q}_{yaw}$ with respect to the body frame $(o_1 x_1 y_1 z_1)$.

The desired path is implicitly defined by two waypoints p_k and p_{k+1}. Moreover, the robot's position in the path fixed coordinate frame is computed by

$$\begin{bmatrix} s(t) \\ e(t) \end{bmatrix} = \begin{bmatrix} \cos(\alpha_k) & -\sin(\alpha_k) \\ \sin(\alpha_k) & -\cos(\alpha_k) \end{bmatrix} \cdot (o_1 - p_{k+1}) \tag{3}$$

where s, e and α_k are the along-track distance, cross-track error and the straight-line angle, respectively. The control objective is to minimize e as follows:

$$\lim_{t \to \infty} s(t) = 0, \quad \lim_{t \to \infty} e(t) = 0 \tag{4}$$

As hexapod robots are omnidirectional vehicles, both sideways motion V_y and rotational motion $\dot{q}_{yaw}$ are used in order to minimize the cross-track error e. The forward velocity V_x is given by

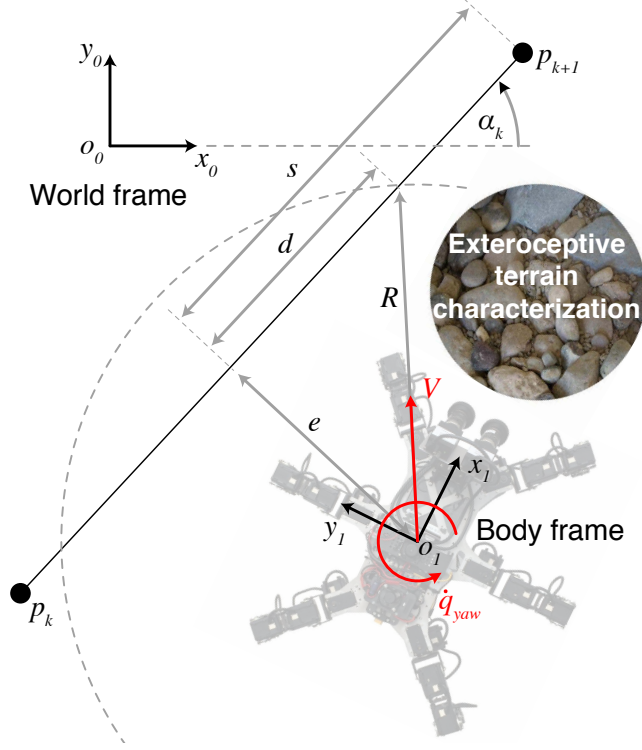$$V_x = V_{x,max} \cdot \frac{s}{\sqrt{s^2 + d^2}} \tag{5}$$

Figure 5: Lookahead-based steering approach based on a straight line path between two waypoints.

where $d = \sqrt{R^2 - e^2}$ and $V_{x,max}$ are the lookahead distance and the maximum along-track velocity. Figure 5 illustrates the radius (R) of the circle of acceptance. There is no intersection between the circle and the path if the robot is too far away from the desired path. In such situations a path planner needs to replan a new path towards the desired goal. The relationship in (5) ensures that the robot ramps down its forward velocity to zero as the along-track distance s approaches zero. The desired sideways motion is given by

$$V_y = \begin{cases} V_{y,max} \cdot \dfrac{e}{|\alpha_e|} & \text{if } |\alpha_e| < \alpha_{e0} \quad \text{(6a)} \\ \\ 0 & \text{otherwise} \quad \text{(6b)} \end{cases}$$

where

$$\alpha_e = \alpha_k - q_{yaw} \tag{7}$$

and α_e is the angle error between the straight line and the robot's orientation. $V_{y,max}$ and α_{e0} are the maximum sideways speed and the range of α_e for which the sideways motion is enabled. The rotational motion is

$$\dot{q}_{yaw} = -K_{rot} \cdot (\alpha_k + \arctan(-\frac{e}{d}) - q_{yaw}) \tag{8}$$

where K_{rot} is the P-Gain of the heading autopilot and $\alpha_k + \arctan(-\frac{e}{d})$ is the desired course angle. If the robot's position at time t satisfies the relationship $||o_1 - p_{k+1}|| \leq R_{next}$, the next straight line segment is selected.

4.2   Leg Motion Control

The following section describes the trajectory generator, impedance controller and inclination controller. These control elements are specifically designed for legged robot motion and were introduced in Bjelonic et al. (2016).
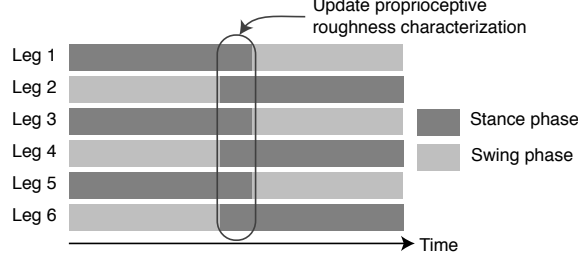
Figure 6: Sequence diagram of the tripod gait for one stride. Update of the proprioceptive roughness characterization requires all 6 foot tips to be in contact with the ground (leg numbers refer to Figure 3).

4.2.1 Stride Trajectory Generator

The velocity commands that are generated by the path follower (Section 4.1.2) are further processed by the stride trajectory generator. The latter generates a gait pattern for all six legs and outputs a reference foot tip trajectory that is fed into the impedance controller (Figure 4).

Hexapod robots move by coordinating the stance and swing phases of the six legs. A stride is the combination of leg movement while the foot tip touches the ground (stance phase) and the swing, moving it in a certain direction (swing phase) within one gait cycle. Legged robots are able to create variable gait patterns by performing different sequences of stance and swing phases. This results in different duty factors $\beta = T_{Stance}/T_{Stride}$ for each gait pattern. Here, $T_{Stride} = T_{Stance} + T_{Swing}$ and the parameters T_{Stance} and T_{Swing} are the durations each leg spends in stance phase and swing phase. In this work the alternating tripod gait is used ($\beta = 0.5$). Three legs are in swing phase and the other three legs are in stance phase. This results in a faster locomotion of the robot with respect to other gaits with a higher duty factor β while static stability is ensured at all time. Figure 6 shows the sequence diagram of the tripod gait.

As shown on the sequence diagram, the foot path planner initiates stance and swing phases for each leg. Further, the desired forward, sideways and rotational motion of the path follower sets orientation and shape of the reference foot tip trajectory $p_{r2} = [x_{r2}\ y_{r2}\ z_{r2}]^T$ with respect to the leg frame ($o_2 x_2 y_2 z_2$). The foot tip trajectory of the swing phase is modelled by a Bèzier curve. The total velocity v of the robot is given by

$$v = \frac{\zeta}{\beta} S_{Stride} f_{Stride} \tag{9}$$

where β, S_{Stride} and $f_{Stride} = 1/T_{Stride}$ are the duty factor, stride length (Figure 3) and stride frequency, respectively. The efficiency of the locomotion ζ depends on the slippage between foot tip and ground ($0 \leq \zeta \leq 1$). Legged robots are able to change their velocity by changing the stride length S_{Stride} or the stride frequency f_{Stride} in (9). In this work the path follower sets the stride length and the adaptation controller adapts the stride frequency based on the terrain structure (Figure 4). This increases the autonomy and efficiency on various terrain types Bjelonic et al. (2017). In addition, the stride height h_{Stride} of the reference foot tip trajectory is adapted by the adaptation controller.

4.2.2 Impedance Controller

Impedance control is a force control method that adds virtual elastic elements to a mechanical stiff configuration. The impedance controller design models the behavior of the foot tip as a virtual mass m_{virt}, virtual stiffness c_{virt} and virtual damper b_{virt} (Bjelonic et al., 2016). Therefore, this design is defined in the Cartesian space of the leg frame ($o_2 x_2 y_2 z_2$). Impedance control achieves a self-stabilizing behavior and energy efficient locomotion by maintaining ground contact without prior profiling of the environment. Thus, this refers to a reactive control approach using proprioceptive sensing.

The force at the foot tip F_z in z_2 direction with respect to the leg frame is transformed into a delta foot tip position Δz_r. This is expressed by the differential equation

$$- F_z = m_{virt}\ddot{\Delta z_r} + b_{virt}\dot{\Delta z_r} + c_{virt}\Delta z_r \tag{10}$$

The reference foot tip trajectory $\mathbf{p_r} = [x_r \ y_r \ z_r]^T$ given by the stride trajectory generator (as described in Section 4.2.1) is adapted by

$$\mathbf{p_d} = \begin{bmatrix} x_r \\ y_r \\ z_r - \Delta z_r \end{bmatrix} \tag{11}$$

Thus, only the z_2 direction is adapted by the impedance controller. On uneven terrain the robot adapts its foot tip position due to impact forces with the ground. The desired foot tip position $\mathbf{p_d}$ and the desired foot tip orientation from the inclination controller (i.e., the angles δ_d and β_d) are further processed by the inverse kinematics. Finally, the desired and current motor positions of the five joints are processed by a PID controller. As described in Section 4.3.3, the adaptation controller in Figure 10 adapts the virtual stiffness c_{virt} in (10) based on terrain perception.

4.2.3 Inclination Controller

The inclination controller sets the desired foot tip orientation for the inverse kinematics and determines a desired pose of the body (Bjelonic et al., 2016). It uses the inclination angles obtained by the proprioceptive terrain estimation. In combination with the inverse kinematics the foot tip is aligned with the gravity vector by specifying the angles δ_d and β_d of the inverse kinematics. Weaver's center of mass (CoM) is shifted to increase the Normalized Energy Stability Margin (NESM) (Hirose et al., 2001) when standing on inclined terrain. Additionally, the pitch and roll angle of the robot's body are adapted. With its novel five DoF leg design Weaver is able to cope with inclination angles in any direction. Thus, Weaver is also able to increase the efficiency and stability even on inclines orthogonal to the to the direction of travel by specifying β_d. The work conducted in Bjelonic et al. (2016) gives a more detailed insight into the inclination controller.

4.3 Terrain Perception for Adaptive Control

While the navigation system in Figure 4 deals with the high-level abstraction of the path, this section concentrates on the low level autonomy of Weaver. Two terrain perception approaches are described, which allow the robot to adapt the motion of each leg. The foot tip trajectory and impedance control, i.e., stride height and stride frequency as well as virtual leg stiffness respectively are adapted. This allows maneuvering of legged robots on previously unknown, challenging terrain types and leads to increased efficiency and stability. The two terrain estimation approaches are based on exteroceptive and proprioceptive perception. They are described in the following sections. Moreover, the system is capable of combining the two perception methods, thus combining reactive and proactive perception. The main contributions of our work stem from proprioceptive terrain perception and extensions of the adaptive control architecture.

4.3.1 Exteroceptive Terrain Perception

Exteroceptive terrain perception is introduced in Homberger et al. (2016) and applied in Bjelonic et al. (2017). Using stereo cameras and an IMU the terrain in front of the robot's walking direction is characterized. Based on this terrain characterization, the adaptation controller sets suitable parameters of the reactive controller, which is described in Section 4.2. As the perception is based on exteroceptive sensing (i.e., stereo camera), this is the proactive element of the hybrid controller in Figure 4.
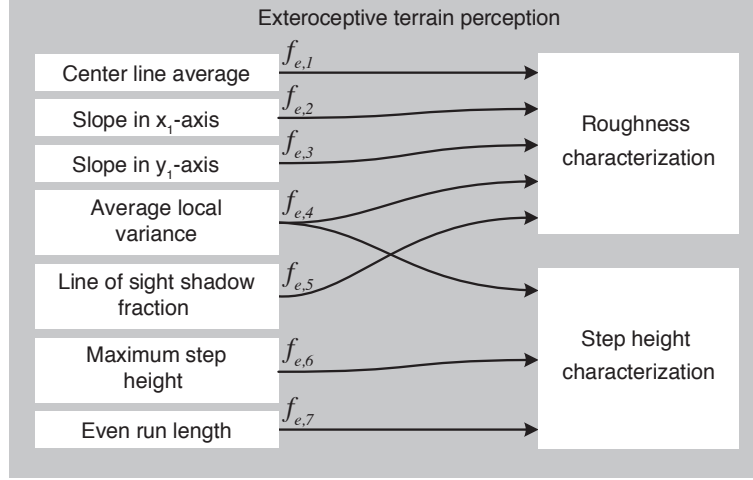
Figure 7: The features $f_{e,i}$ used within the exteroceptive terrain perception module are further processed to generate descriptive parameters for roughness r_e and step height h_e characterization.

Using the stereo disparity information of the upcoming surface, a point cloud in 3D space is generated. The IMU signal is used to align the point cloud with the direction of the gravity vector. After generating a Digital Elevation Model (DEM) of this data, several terrain intrinsic features $f_{e,i}$ are extracted therefrom. These features are listed in Figure 7. A complete description of the exteroceptive terrain feature extraction can be found in Homberger et al. (2016).

As illustrated in Figure 7, the features $f_{e,i}$[1] are further processed to generate descriptive parameters for roughness and step height characterization. Both parameters are input to the adaptation controller and reflect the properties of the terrain in front of Weaver. The roughness parameter $r_e \in [0, 1]$ which characterizes the unevenness of the terrain is given by

$$ r_e = \frac{1}{r_{e,max}} \sum_{i=1}^{5} a_{e,i} \cdot f_{e,i} \tag{12} $$

The step height parameter $h_e \in [0, 1]$ depicts the maximum difference of the terrain's height elevation. This parameter is calculated by

$$ h_e = \frac{1}{h_{a,max}} (a_{e,6} \cdot f_{e,6} + a_{e,7} \cdot f_{e,4} \cdot f_{e,7}) \tag{13} $$

where the weighting parameters $a_{e,i}$ for both terrain parameters are set empirically for a number of exemplary terrain types. By this means, the weighting parameters are robot specific and indicate how much the terrain features influence the overall roughness and step height characteristics. Depending on the capabilities of the robot some of the terrain features should be penalized more with respect to other features by setting a higher weight. The term $a_{e,7} f_{e,4} f_{e,7}$ of the step height h_e quantifies the occurrence of nearly planar surfaces which are bordered by steep slopes. Further, r_e and h_e are normalized between zero and one by dividing both terrain parameters by a virtual maximum value occurring on highly challenging terrain. This exemplary terrain type gives the highest values $r_{e,max}$ and $h_{e,max}$. Both values are platform specific and must be updated for different platforms since the maximum roughness and step height depends on factors such as the robot's size. If the roughness or step height characteristics exceed their critical value, the roughness or

---

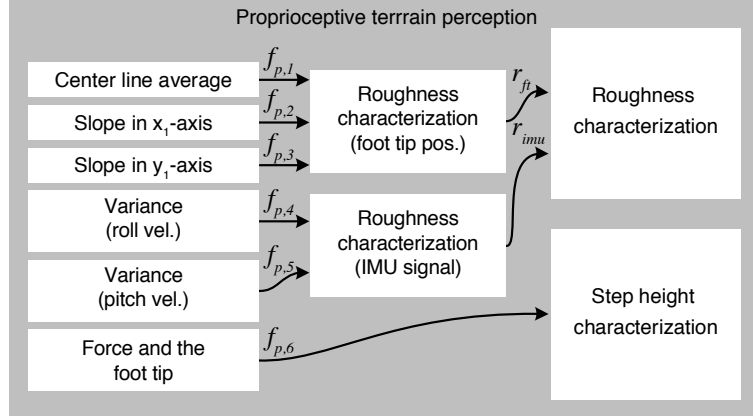[1] The subscript e stands for exteroceptive.

Figure 8: The features $f_{p,i}$ used within the proprioceptive terrain perception module are further processed to generate descriptive parameters for roughness r_p and step height h_p characterization.

step height value is set to 1. Moreover, the roughness and step height parameters are synthetic metrics that integrate physical values but have no physical meaning anymore.

As the robot perceives terrain features at a given distance in front of the robot (in its heading direction), information on ego-motion is needed (Figure 5). The body trajectory and orientation given by the visual-inertial odometry are used to update a spatial map of roughness and step height values with respect to the world frame. A circular area around the center of the body frame which contains the relevant area for the robot's foot tip placement is searched for the highest roughness and step height values. From these the highest values of r_e and h_e are selected, i.e., the set of terrain characteristics which lead to the most conservative control actions are determined. On one hand, this ensures that the robot can safely traverse the given area but on the other hand, this also reduces the performance in terms of speed. Nevertheless, safe locomotion of the robot is considered more important than higher speed, as the latter may cause an unstable walking configuration. The next section shows a reactive approach to characterize the terrain using proprioceptive sensing only.

4.3.2 Proprioceptive Terrain Perception

The following method consists of using only proprioceptive sensing to obtain information about the terrain structure. The robot needs to walk on the terrain in order to perform the sensing, in a purely reactive approach. The algorithm uses the feedback of the IMU and the motors of each joint. Moreover, both feedback signals are combined to enhance the estimate of the terrain properties.

An overview of the proprioceptive terrain perception is depicted in Figure 8. A set of proprioceptively acquired measurements $f_{p,i}$[2] are combined to generate roughness characterization r_p and step height characterization h_p of the terrain. The roughness characterization is split into two separate stages. The first roughness characterization r_{ft} depends on the foot tip positions, which are considered to be a sparse subsample of the underlying terrain. In the second stage, roll and pitch angular velocity readings of the IMU are used to generate the roughness characterization r_{imu}.

As both of these methods are leading to a wrong roughness estimation if applied separately, they are combined for increased reliability. The foot tip position based roughness characterization is most meaningful if the virtual leg stiffness is low as the foot tips can be flexibly adapted to a given rough terrain. However, this is not possible if the leg joints are stiff. On the other hand, the angular velocity measurements are more expressive if virtual stiffness is high as flexible legs lead to low body angular velocity on any terrain type

---

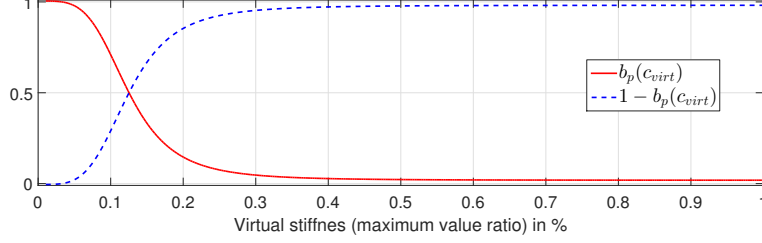[2]The subscript p stands for proprioceptive.

Figure 9: Symmetrical sigmoidal function defines the weighting between both proprioceptive roughness estimates with respect to the current virtual stiffness of the impedance controller.

(Bjelonic et al., 2016). So there is no distinction between flat and uneven terrain possible. Therefore the two approaches are weighted by the currently applied virtual stiffness value.

The position of each foot tip is determined by forward kinematics. These Cartesian positions are used to generate a terrain model by incorporating the relative position of each foot tip and the orientation of the body with respect to the gravity vector. This terrain model is updated at every moment in time where all six legs are in stance phase. See Figure 6 for the exact timing of this roughness update. Using an IMU the six foot tip positions are transformed into a coordinate system which is aligned with the gravity vector. This allows terrain intrinsic feature extraction as shown by Homberger et al. (2016). A plane is fit through the six positions p_i using the least squares error method. The plane equation is given by

$$z = a \cdot x + b \cdot y + c \tag{14}$$

where $[x\ y\ z]^T$ is a point on the plane and the parameters a, b and c are determined by the least square fit. The generated plane is used to calculate the center line average given by

$$f_{p,1} = \frac{1}{6} \sum_{i=1}^{6} |z_i - z_{plane}| \tag{15}$$

where z_i is the vertical position of the foot tip with respect to the gravity aligned coordinate system and z_{plane} is the vertical position of the corresponding point of the fitted plane (i.e., $x_{Plane} = x_i$ and $y_{Plane} = y_i$). The fitted plane is used to derive the mean inclination angles of the terrain $f_{p,2}$ and $f_{p,3}$. In addition these angles are used in the inclination controller described in Section 4.2.3. Similar to the exteroceptive roughness estimation in (12) the proprioceptive roughness estimation $r_{ft} \in [0,1]$ using the foot tip position is given by

$$r_{ft} = \frac{1}{r_{p,max}} \sum_{i=1}^{3} a_{p,i} \cdot f_{p,i} \tag{16}$$

The variance of the roll $f_{p,4}$ and pitch velocity $f_{p,5}$ are updated over a predefined time range. Both are combined in a single estimate of the roughness $r_{imu} \in [0,1]$ given by

$$r_{imu} = \frac{1}{r_{p,max}} \sum_{i=4}^{5} a_{p,i} \cdot f_{p,i} \tag{17}$$

where the weighting parameters $a_{p,i}$ and the highest roughness value $r_{p,max}$ of the proprioceptive estimation are set empirically similarly as for the exteroceptive estimation in Section 4.3.1. Both roughness estimations in (16) and (17) are combined to improve the terrain perception and to avoid the two cases explained above. The final roughness estimate $r_p \in [0,1]$ is derived by

$$r_p = b_p(c_{virt}) \cdot r_{ft} + (1 - b_p(c_{virt})) \cdot r_{imu} \tag{18}$$

where $b_p(c_{virt})$ is a gain that defines the weighting of both roughness estimates r_{ft} and r_{imu} with respect to the current virtual stiffness c_{virt} of the impedance controller. The gain $b_p(c_{virt}) \in [0,1]$ is a function that

weighs the estimation from the foot tips higher than the estimation from the IMU when walking with low virtual stiffness and vice versa for locomotion with high virtual stiffness. Figure 9 shows the symmetrical sigmoidal function that is used in our work to achieve the weighting between both estimates. It can be seen that adaptation of the foot tip positions is only achieved for low virtual stiffness values. Therefore, the function $b_p(c_{virt})$ already switches to the roughness estimate from the IMU after 0.13 times the highest virtual stiffness value of the adaptive controller. Depending on the robot and task an arbitrary function for $b_p(c_{virt})$ can be chosen. We use the sigmoidal function due to the steep and continuous shape around the roughness estimation change.

A further extracted proprioceptive feature is the force difference at the foot tip $f_{p,6}$. Moreover, the tangential force $F_t = (F_x^2 + F_y^2)^{1/2}$ calculated through the Jacobian in (1) is stored over a predefined time span. The feature $f_{p,6}$ is the absolute difference between the maximum and minimum force F_t. The step height characterization in Figure 8 uses this feature to estimate the step height h_p of the terrain. Without any exteroceptive measurements, the robot is just able to perceive steps in the terrain by interacting with the environment. If the feature $f_{p,6}$ is greater than a tuned heuristic threshold σ_f, the step height estimate of the terrain increases. Similarly, the stride height h_{Stride} of the foot increases by h_p after the interaction. In addition, the proprioceptive step height estimation incrementally reduces the stride height by h_p if the tangential force stays below the threshold σ_f for a predefined time range. This enables the robot to estimate the step height by incrementally increasing or decreasing the stride height of the foot tip and analyzing the torque measurements of each motor. The implementation of the step height estimation can be obtained in Algorithm 1. The next section describes adaptation mechanism in more detail.

Algorithm 1 Proprioceptive step height estimation.

1: **procedure** STEPHEIGHTESTIMATION
2:      *initialization*:
3:      $t_{inc} \leftarrow$ time of last step height increase
4:      $t_{dec} \leftarrow$ time of last step height decrease
5:      $\Delta t \leftarrow$ time of next step height change
6:      $\sigma_f \leftarrow$ force threshold
7:      $h_{add} \leftarrow$ step height increment
8:      $h_p \leftarrow$ step height
9:      $h_{max} \leftarrow$ maximum step height
10:     *loop*:
11:     $f_{p,6} \leftarrow$ tangential force difference
12:     $t_{now} \leftarrow$ current time
13:     **if** $f_{p,6} > \sigma_f$ **and** $t_{now} - t_{inc} > \Delta t$ **then**
14:         $t_{inc} \leftarrow t_{now}$
15:         $h_p \leftarrow h_p + h_{add}$
16:         **if** $h_p > h_{max}$ **then**
17:             $h_p \leftarrow h_{max}$
18:             **close**
19:         **close**
20:     **else if** $t_{now} - t_{inc} > \Delta t$ **and** $t_{now} - t_{dec} > \Delta t$ **then**
21:         $t_{dec} \leftarrow t_{now}$
22:         $h_p \leftarrow h_p - h_{add}$
23:         **if** $h_p < 0.0$ **then**
24:             $h_p \leftarrow 0.0$
25:             **close**
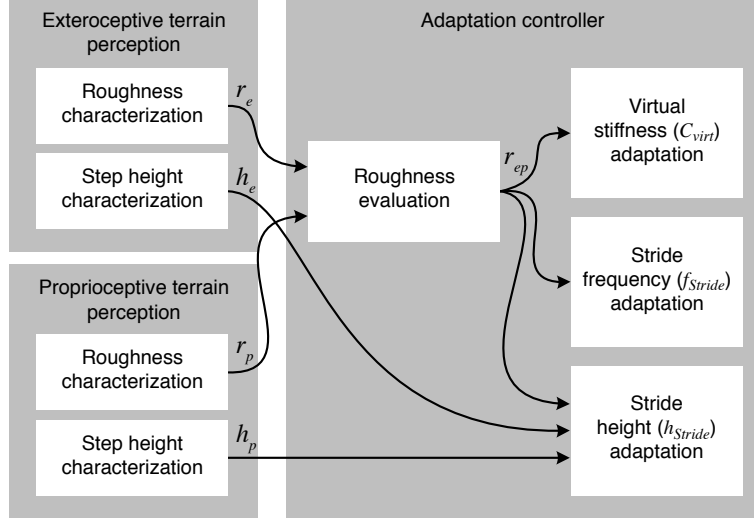26:   **close**
27:     **goto** *loop*

Figure 10: Functional components of the adaptation controller and its connectivity with the perception modules.

4.3.3 Adaptive Control using Exteroceptive and Proprioceptive Sensing

Bjelonic et al. (2017) shows that locomotion on varying terrain requires adaptive control and motion parametrization. An optimized parameter set for the traversed terrain increases the efficiency and stability of the locomotion. In contrast, a wrong choice of the parametrization may lead to mission failure. Adaptive control using exteroceptive and proprioceptive terrain estimation is proposed to improve the locomotion on varying terrain. The main contribution of our work focuses on the combined usage of both terrain estimations in situations where the exteroceptive perception system is not able to identify the characteristics of the terrain. Adaptive control requires the feedback of the control output and this is covered by the proprioceptive terrain estimation since it uses feedback from the motors and the IMU (Figure 4). In contrast, the exteroceptive terrain estimation can be interpreted as a feed-forward element of the adaptive controller since no state is fed back from the robot. Figure 10 shows the control architecture of the adaptation controller.

The roughness characterizations with exteroceptive sensing r_e and proprioceptive sensing r_p are combined in a single estimate of the roughness r_{ep}[3] by using the following condition

$$r_{ep}(r_e, r_p) = \begin{cases} r_e & \text{if } |r_e - r_p| < \sigma_r \quad\quad\quad\quad (19\text{a}) \\ r_p & \text{otherwise} \quad\quad\quad\quad\quad\quad\quad (19\text{b}) \end{cases}$$

where σ_r is a threshold of the roughness error $|r_e - r_p|$. In most cases the exteroceptive perception yields more information and is more stable since the proprioceptive perception relies on a sparse subsample of the traversed terrain, given by six Cartesian positions of the foot tips. Furthermore, the exteroceptive estimation perceives the terrain properties proactively, whereas the proprioceptive approach enables the robot to instantaneously react to changes of the terrain only. In cases where the error term $|r_e - r_p|$ is exceeding the threshold σ_r, the robot switches to the proprioceptive terrain perception. This occurs in areas where the robot is not able to model the terrain using its exteroceptive sensing (e.g., high grass, bad illumination, motion blur and dynamic scenes).

Similar to the terrain characterization, the adaptation in Figure 10 uses the derived roughness r_{ep} of the terrain to adapt the virtual stiffness c_{virt} (10) and the stride frequency f_{Stride} (9). The adaptation is defined by

---

[3]The subscript ep stands for the combined exteroceptive and proprioceptive roughness estimation.

$$c_{virt} = b_0 + b_1 \cdot r_{ep} + b_2 \cdot r_{ep}^2 + b_3 \cdot r_{ep}^3 \tag{20}$$

$$f_{Stride} = c_0 + c_1 \cdot r_{ep} + c_2 \cdot r_{ep}^2 \tag{21}$$

The adaptation of the stride height h_{Stride} relies on the step height h_e of the exteroceptive terrain estimation and the step height h_p of the proprioceptive estimation. The adaptation of the stride height is given by

$$h_{Stride} = d_0 + d_1 \cdot h_e + d_2 \cdot r_{ep} + h_p \tag{22}$$

The parameters b_i, c_i and d_i are the coefficients of polynomial functions. These functions are derived empirically for a number of exemplary terrain types. By this means, the roughness r_{ep} and step height h_e are measured for various terrain structures similar to the terrain segments shown in Section 5 (Bjelonic et al., 2017). Polynomial functions are fitted through the data points, which are the tuples consisting of terrain characterization parameters (r_{ep} and h_e) and their corresponding desired (optimal) adaptation parameters (c_{virt}, f_{Stride} and h_{Stride}). A least square fit yields the coefficients of the polynomials that are used in (20), (21) and (22). Furthermore, the proprioceptive estimation of the step height h_p is added directly to (22) since, in contrast to the other terrain characteristics, h_p is not dimensionless. A few number of terrain types are needed to generate feasible polynomial functions that generalize to unseen environments. By this means, the curve fit enables the robot to be applicable to many different terrains and there is no need to handcraft different adaptation parameters for different applications.

4.3.4 Adaptation Approaches for Experimental Evaluation

In order to evaluate the performance of the adaptive controller, we distinguish between four different adaptation approaches; namely non-adaptive, exteroceptive-adaptive, proprioceptive-adaptive and combined-adaptive control. The non-adaptive controller is simply setting a constant virtual stiffness c_{virt}, stride frequency f_{Stride} and stride height h_{Stride}. In contrast, the remaining adaptation approaches are based on Section 4.3.3. Exteroceptive-adaptive control is only based on the terrain perception in Section 4.3.1, i.e., $h_p = 0$ and $r_{ep} = r_e$. Proprioceptive-adaptive control is only based on the terrain perception in Section 4.3.2, i.e., $h_e = 0$ and $r_{ep} = r_p$. Finally, combined-adaptive control leverages from both terrain perceptions by applying (20), (21) and (22).

5 Experiments

A number of experiments were conducted to compare the performance of previously presented control algorithms in terms of energy efficiency, locomotion velocity and body stability.

5.1 Experimental Setup

To generate comparable experimental results in variable environments, a multi-terrain testbed was built and is illustrated in Figure 11. The robot starts on flat ground (segment A) and then passes an inclined planar slope (segment B) before entering rough terrain (segments C to F). Segment C of the testbed contains wooden blocks of various heights and segment D-E-F is a mixture of sand, pebbles, river stones, crumbled concrete and bigger stones. The robot finishes its run on a patch of flat terrain. A different view of segments C and D is shown in Figure 1(a).
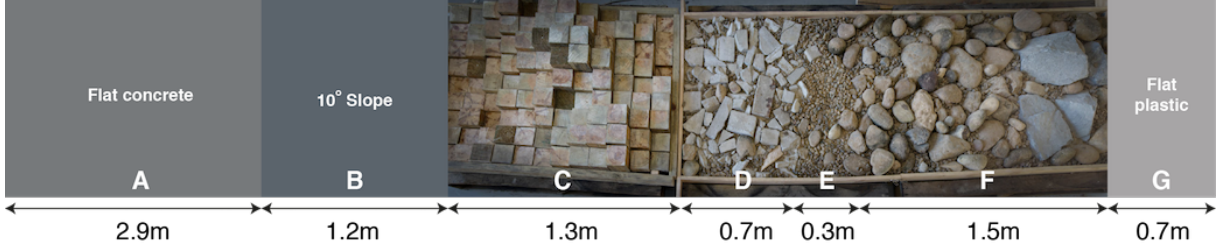
Figure 11: Multi-terrain testbed with maximum height difference: 113% (segment C), 28% (segment D), 11% (segment E) and 72% (segment F) of Weaver's ground clearance height ($0.2\,\text{m}$). The width of the testbed is 145% of Weaver's start-up width ($0.63\,\text{m}$). Total length of the testbed is $8.6\,\text{m}$ and Weaver's length is $0.62\,\text{m}$.

The robot used visual-inertial odometry and the navigation system described in Section 4.1 to autonomously move along predefined waypoints without any prior information about the environment. The power consumption P was measured at $20\,\text{Hz}$ by the Arduino based current sensor. The robot's velocity v was calculated by tracking its position at $4\,\text{Hz}$ using a robotic total station (Leica TS12) with a target prism mounted on the robot. The robot's position data obtained in this manner was only used for ground truth and was not used in its control. All parameters used throughout the experiments are summarized in Appendix A. Throughout the experiments we used one parameter set for the adaptation modules and we did not change the parameters depending on the travelled terrain.

5.2   Multi-terrain Testbed Experiments

For this experiment, Weaver autonomously navigates along a straight line defined by two waypoints over the multi-terrain testbed (Figure 11). Three sets of 15 runs each were conducted to compare the performance using the exteroceptive-adaptive, proprioceptive-adaptive and non-adaptive controller (Section 4.3.4). The experimental sets are therefore referred to as exteroceptive-adaptive, proprioceptive-adaptive and non-adaptive set, respectively. The parameter set of the non-adaptive controller is tuned to roughly match the locomotion behavior of the exteroceptive-adaptive controller on the roughest terrain part (segments C to F).

5.3   Outdoor High Grass Experiments

Similar to the previous experiment, Weaver autonomously follows a straight line in outdoor terrain, as shown in Figure 1(b). This terrain consists of high grass with underlying uneven and almost even ground. Two sets of 5 runs were conducted to evaluate the performance using the combined terrain estimation of the exteroceptive and proprioceptive sensing. This experiment considers the scenario in which the cameras are unable to perceive the relevant terrain structure, as the scene is obstructed by high grass. Weaver's ability to cope with these environments using combined-adaptive control is evaluated against exteroceptive-adaptive control (Section 4.3.4). These experimental sets are referred to as combined-adaptive set and exteroceptive-adaptive set respectively.

5.4   Performance Criteria

The dimensionless energetic cost of transport (CoT) is a common performance metric used for comparing energy efficiency for ground robots (Bjelonic et al., 2016, Kottege et al., 2015). The instantaneous cost of transport CoT and the averaged cost of transport over a travelled distance $\overline{CoT}$ are defined as

$$CoT = \frac{UI}{mgv}, \quad \overline{CoT} = \frac{\frac{1}{n}\sum\limits_{i=1}^{n} U_i I_i}{mg\frac{\Delta x}{\Delta t}}, \tag{23}$$

where U is the voltage of the power supply, I is the instantaneous current drawn from the power supply, m is the mass, g is the gravitational acceleration, v is the instantaneous velocity of the robot and Δt is the time needed to travel distance Δx. The CoT captures the overall energy consumption of the robot based on the voltage and current of the power supply. This includes mechanical power and losses, e.g., due to friction. The energy efficiency highly depends on the characteristics of the servomotors (e.g., internal PID gains, resistance, induction, reduction ratios). Since this work compares the CoT of different control algorithms on the same robotic platform, it is assumed that the influence of these characteristics remain unchanged during experimentation. However, it should also be noted that the overall power consumption of the robot includes the processing of the two on-board PCs, which require approximately 50 W each during operation. In all experiments the vision-based processing including the exteroceptive terrain estimation is enabled. We therefore focus on the evaluation of the different adaptation algorithms with respect to the locomotion performance.

Another performance indicator, *percentage reduction in variance*, is used to assesses the stability of the robot's body. This is based on the angular body movement and is used in the field of ship control assessment (Perez, 2005). The percentage reduction of variance S_i is given by

$$S_i = 100 \cdot \left(1 - \frac{Var(X_{i,a})}{Var(X_{i,na})}\right) \tag{24}$$

where i is a place holder for the movement in pitch and roll. The function $Var(\cdot)$ is the variance and the variable X_i is the set of observed values in radians. The subscripts a and na stand for adaptive and non-adaptive respectively. Maximizing (24) leads to reduced limit cycles of the angular body trajectory and therefore the robot stays inside of its basin of attraction. As shown by Goswami et al. (1998), the orbital stability of the robot is herewith proven.

6   Results

The following sections summarize the results from the experiments on the multi-terrain testbed, and outdoors in high grass[4].

6.1   Experiments on the Multi-Terrain Testbed

This section compares the performance results of the non-adaptive and the adaptive control algorithms in experiments on the multi-terrain testbed. These experiments have been conducted to compare the efficiency of non-adaptive and adaptive control. As can be seen in Bjelonic et al. (2016), a non-adaptive controller tuned to match the locomotion of the adaptive controller on flat terrain (segment A) is incapable of finishing the terrain task in rough terrain. In the following the evolution of the CoT and the angular body movement as well as the performance of the navigation system on rough and variable terrain are presented.

Figure 12 shows the CoT (upper figure) and the corresponding adaptation parameters (lower figure) for all three controllers. The lines in the upper figure depict the mean CoT of the 15 runs whereas the grey shading visualizes one standard deviation of the CoT of the exteroceptive-adaptive set. Adaptation based on exteroceptive sensing achieves the lowest CoT on the multi-terrain testbed. It is lower than the CoT of the proprioceptive-adaptive set. This can be explained by the more anticipative character of the exteroceptive sensing. That is, the exteroceptive sensing relies on the topology of a terrain patch in front of the robot's

---

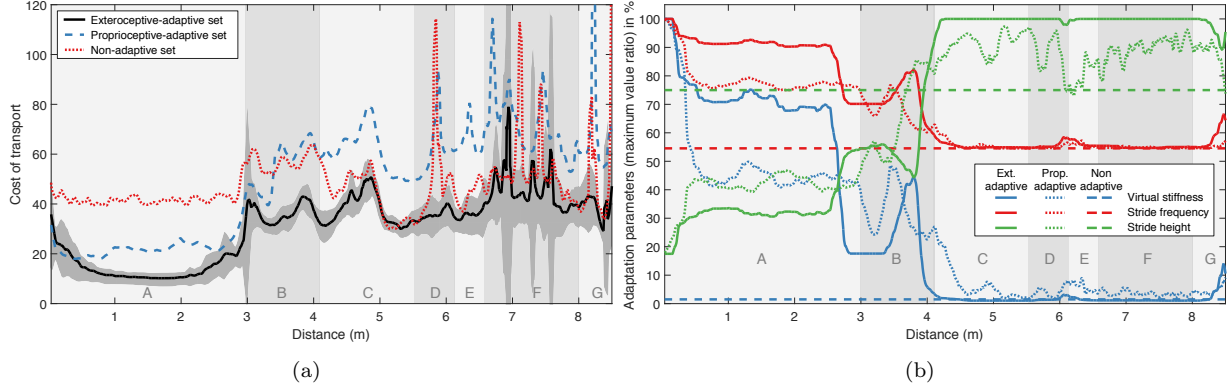[4]Videos of the experiments are available online at https://research.csiro.au/robotics/weaver/

Figure 12: The CoT of the exteroceptive-adaptive, proprioeptive-adaptive, adaptive, non-adaptive controller shows the results of 15 runs each on the multi-terrain testbed; (a) The black line and the grey shading are the mean and one standard deviation of the CoT of the exteroceptive-adaptive set and the blue and red line shows the mean of the CoT of the proprioceptive-adaptive and non-adaptive set respectively. (b) The percentage values of adaptation parameters are shown. The solid lines are the mean parameters of the exteroceptive-adaptive set, the dotted lines are the mean parameters of the proprioceptive-adaptive set and the dashed lines show the values of the non-adaptive approach.

walking direction whereas the proprioceptive sensing relies on the terrain patch the robot is currently walking on. The latter method yields a jittering evolution of the adaptation parameters, especially for instantaneous changes of terrain type. The exteroceptive control method therefore performs better in terms of body velocity, angular body movement and stability. Nevertheless, the exteroceptive- and proprioceptive-adaptive sets achieve similar adaptation parameters for the different terrain types of the multi-terrain testbed. Therefore, the two adaptation methods clearly show an advantage over the non-adaptive approach of having fixed controller gains on varying terrain. The robot with non-adaptive control is able to traverse the challenging terrain (Segment C to F) but this parametrization increases the CoT on flat terrain (Segment A and B) with respect to both adaptive sets. The exteroceptive-adaptive and non-adaptive set achieve similar results on the rough terrain (Segment C to F). In contrast, the non-adaptive controller outperforms the proprioceptive-adaptive controller in this type of terrain. This result is also reasonable since the non-adaptive controller is tuned for the rough terrain. This result can also be obtained from Appendix B. Nevertheless, both adaptive sets have a higher stride height on rough terrain. This shows that the stride height is not influencing the CoT as much because the robot is able to traverse the height differences of the terrain with both stride height parameterizations. This would change if the height difference of the terrain would increase.

Both virtual stiffness and stride frequency are more critical for the performance of the robot. Homberger et al. (2016) shows the influence of only virtual stiffness adaptation. Comparison with this work shows that the CoT is even more reduced on the flat terrain with the adaptation of the stride frequency. An optimized parameter set with respect to the flat terrain (Segment A) of the non-adaptive controller implies that the robot is not able to traverse the uneven terrain (Segment C to F) without adapting the controller gains (Bjelonic et al., 2016). The average CoT over the multi-terrain testbed are 36.43 ± 1.68 (exteroceptive-adaptive set), 43.00 ± 1.99 (proprioceptive-adaptive set) and 51.74 ± 3.46 (non-adaptive set). Therefore, the exteroceptive-adaptive and propriceptive-adaptive controller reduce the overall CoT with respect to the non-adaptive set by $29.59\,\%$ and $17.89\,\%$ respectively. On flat terrain the minimum CoT (containing all energy losses) of the exteroceptive-adaptive controller is approximately 10 and the maximum velocity is $0.35\,\mathrm{m/s}$.

Figure 13 summarizes the limit cycles of the angular body movement projected onto the phase plane of all runs and Appendix B shows the percentage reduction of variance of the roll and pitch angle for each segment of the terrain. The roll and pitch movement is distinctly reduced in segment A by both adaptive approaches (upper and middle row) with respect to the non-adaptive set (lower row). Similarly the angular pitch velocity is reduced in segment B. For the remaining part of the testbed (segment C to F), on average

the angular movement is reduced by the exteroceptive adaptation controller. This shows that the parameter set of the controller affects the movement of the body on flat terrain and on unstructured terrain. Walking with a low virtual stiffness induces angular body movements on flat terrain (segment A) due to the added virtual elastic behavior (Bjelonic et al., 2016). Conversely, walking with a high virtual stiffness, low stride height and high stride frequency reduced the stability of the robot in unstructured terrain (segment C to F).

The navigation system with the visual inertial odometry and the path follower effectively reduces the error between the desired path and the robot's trajectory. Therefore, it prevents the robot stepping out of the testbed during experimentation. The robot was able to traverse the multi-terrain testbed 45 times. The drift of the odometry is 4 ± 1.9 % with respect to the travelled distance. The error propagation of the odometry is also evaluated in Bjelonic et al. (2017).

The experiment on the multi-terrain testbed shows that the proactive behavior of the exteroceptive-adaptation controller is superior over the proprioceptive-adaptation controller. However, the error $|r_e - r_p|$ in (19a) is not exceeding the threshold σ_r and therefore, a combined-adaptation controller has the same performance like the exteroceptive-adaptation controller. The next experiment shows the value of the combined-adaptation controller in situations where the stereo camera is not able to perceive the environment.

6.2   Outdoor Experiments in High Grass

This section compares the performance results of the non-adaptive and the adaptive control algorithms in outdoor experiments in high grass. These experiments serve as an example for situations where the camera is not able to predict the terrain surfaces accurately.

Figure 14 shows the CoT (a) and the corresponding adaptation parameters (b) for both controllers. The lines depict the mean CoT of the 5 runs whereas the grey shading visualizes one standard deviation of the CoT of the combined-adaptive set. In this experiment the robot starts on flat plastic (segment A), enters uneven grassy terrain (segment B) and finishes its run in even grassy terrain (segment C). As can be seen in Figure 1(b) the height of the grass is similar to the robot's body height. The exteroceptive-adaptive set shows that the robot is not able to differentiate between segment B and C. Moreover, the stereo camera characterizes both terrains as uneven because the ground is covered by grass. Thus, the system with only exteroceptive perception is not able to sense the terrain surface the robot is walking on. In contrast, the combined-adaptive set is able to differentiate between the uneven (segment B) and almost even terrain (segment C). In segment B the exteroceptive and proprioceptive sensing have similar values for the roughness of the terrain and thus the adaptation controller in Section 4.3.3 uses the exteroceptive roughness estimation. In segment C of the outdoor terrain the robot switches to the proprioceptive estimation of the roughness because the roughness error $|r_e - r_p|$ in (19a) exceeds the predefined threshold σ_r. As can be seen in Figure 14, this results in a new parameter set of the virtual stiffness and stride frequency that reduces the CoT with respect to the exteroceptive-set. Interestingly, the stride height remains the same for segments B and C, since the combined-adaptive controller is detecting obstacles due to the resistance of the grass during walking. That is, the robot increases its stride height to minimize the resistance force acting on each leg.

7   Discussion

Weaver is able to autonomously navigate rough terrain by defining a minimal representation of the environment in the form of a roughness and a step height characterization. This enables the robot to find an optimized parameter set (i.e., virtual stiffness, stride height and stride frequency) depending on the terrain the robot is walking on. The adaptation method is based on online exteroceptive and proprioceptive terrain perception and thus, does not require any prior information of the environment. The results show how the CoT and the body movement is affected on different parameter sets in varying terrain.
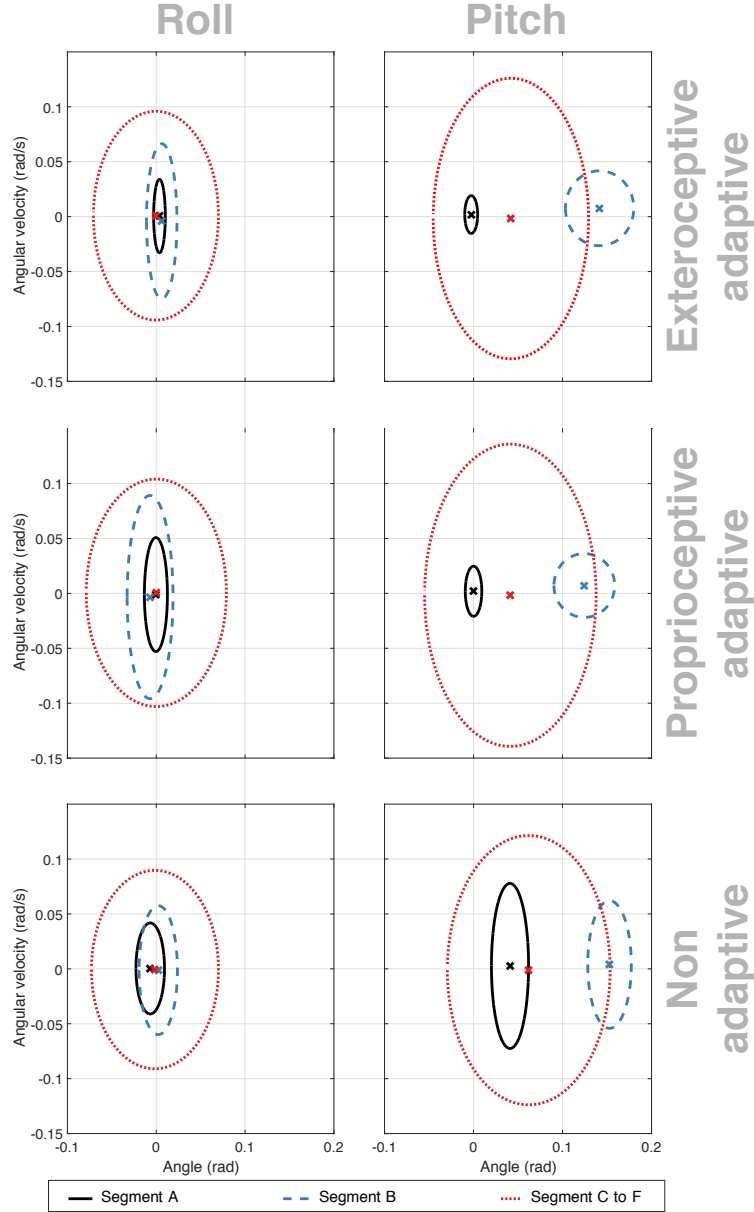
Figure 13: Mean (x) and one standard deviation (ellipse) of the limit cycles of the roll and pitch movement projected onto the phase plane during traversal on the multi-terrain testbed. The upper, middle and lower figure summarize the results of exteroceptive-adaptive, proprioceptive-adaptive and non-adaptive set. The size of the ellipses is an indication of how much the free-floating base moves during the locomotion on the different terrain segments. As shown by Goswami et al. (1998), the size of limit cycles of the angular body trajectory is an indication for the orbital stability of the robot. Reducing the size of the ellipses is favourable in terms of stability. Appendix B complements this figure by showing the percentage reduction of variance of the roll and pitch angle for each segment of the terrain.

Non-adaptive control is useful if the robot is walking on the same terrain type and not entering varying terrains. Moreover, non-adaptive control in varying terrain causes the CoT and body movement to increase with respect to the adaptive approach. The robot may get stuck in challenging terrain when walking with an optimized parameter set for flat terrain and adaptive control outperforms non-adaptive control in varying terrain significantly. Three different kind of adaptation approaches are evaluated on the multi-terrain testbed
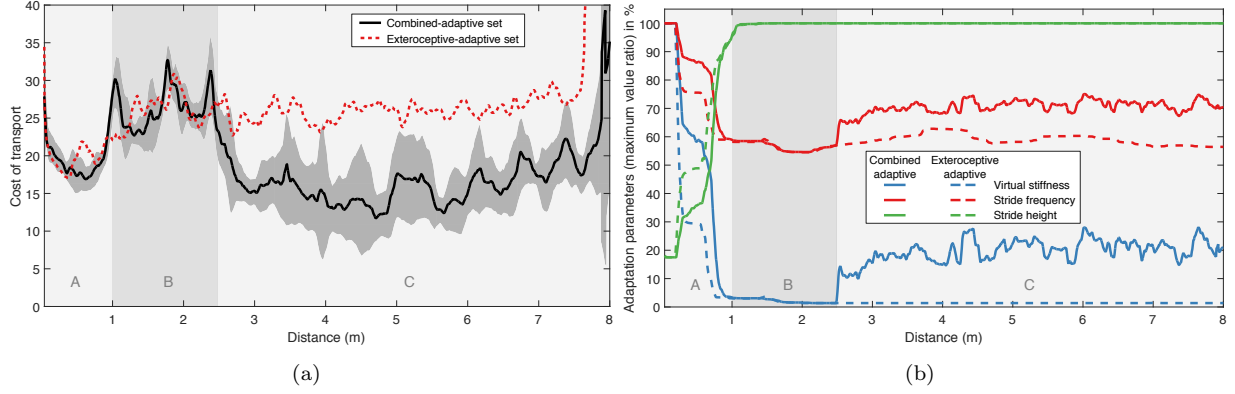
Figure 14: The CoT of the combined-adaptive and exteroceptive-adaptive controller shows the results of 5 runs each in high grass; (a) The black line and the grey shading are the mean and one standard deviation of the CoT of the combined-adaptive set and the red line shows the mean of the CoT of the exteroceptive-adaptive set. (b) The percentage values of adaptation parameters are shown. The solid lines are the mean parameters of the combined-adaptive set and the dashed lines are the mean parameters of the exteroceptive-adaptive set.

and in otdoor terrain: Exteroceptive-adaptive, proprioceptive-adaptive and combined-adaptive control.

Adaptation based on only stereo vision (i.e., exteroceptive-adaptive control) enables Weaver to choose the optimized parameter set in advance since the stereo camera is sensing the terrain in front of the robot. This has several advantages as compared with the proprioceptive-adaptive controller. The exteroceptive-adaptive controller achieves the best performance on the multi-terrain testbed in Section 6.1 since the robot is changing the adaptation parameters in advance. Nevertheless, this approach requires additional payload due to the stereo camera and the computational power increases dramatically (i.e., an additional on-board PC is required). The results in Section 6.2 where the robot is walking in outdoor terrain show also another fundamental problem of exteroceptive sensing. The stereo camera is not able to perceive the structure of the terrain because the surface is covered by high grass that blocks the line of sight of the stereo camera. Difficulties may also arise from bad illumination, motion blur and dynamic scenes. In these situations the proprioceptive-adaptive controller is superior to the exteroceptive-adaptive controller. Moreover, the combined-adaptive controller enhances the locomotion of the robot by combining the advantages of both terrain estimations. The roughness evaluation in (19a) switches to the proprioceptive terrain estimation if the error between the exteroceptive and proprioceptive roughness exceeds a predefined threshold. The proprioceptive-adaptive controller on the other hand is cheap since it does not require additional hardware components. One drawback of the proprioceptive estimation of the roughness and step height is the jittering behavior since it requires interaction with the environment to react to changing terrain types.

The disadvantage of all three adaptation approaches is the parameter tuning of the empirically generated functions inside the perception and adaptation modules. We define adaptation functions for the virtual stiffness, stride height and stride frequency as a weighted linear combination of terrain features. A significant amount of effort needs to be spent in designing these features and the tuning of their weights requires experience. This can be avoided by adapting the approach in Kalakrishnan et al. (2009) for our purpose. The authors describe an alternative approach that can learn a ranking function for rough terrain. However, the parameter tuning is only needed once for every robot and there is no need to adapt the parameter set depending on the application. During the experiments in this work we used the same parameter set for every terrain. The parameters of the adaptation module were obtained through experiments on the terrain segments A, B and C in Figure 11 and this parametrization was able to generalize on the terrain segments C to G in Figure 11 and in the outdoor environment.

The robot is able to reach a waypoint by combining visual-inertial odometry with a path following algo-

rithm based on lookahead-based steering. This framework is suitable for teleopration and semi autonomous navigation where a user specifies safe paths given the on-board sensor feedback. In addition, the waypoint generation through the user can be replaced by a path planner similar to the work of Wermelinger et al. (2016). Furthermore, the global path can also be set in advance in industrial inspection applications where the travelled path of the robot is known in advance. The local terrain estimation using the foot tip positions is used to generate the inclination angles of the terrain. The results in Bjelonic et al. (2016) show that Weaver is increasing the maximum inclination angle and decreasing the CoT on inclined terrain by adapting the five DoF leg configuration. In rough terrain the orientation of the terrain elevation with respect to the robot's body frame changes in roll and pitch direction. The unique 5 DoF leg configuration enables Weaver to cope with inclination angles in any direction due to the possibility to set two desired orientation of the foot tip. On inclined terrain the leg orientation adapts in order to align the gravitational force with the highest singular value direction of the force ellipsoid. This reduces the torque in each motor because the gravitational force is supported with the least amount of effort.

8   Conclusions

This paper describes autonomous navigation and adaptation based on the terrain for a fully self-contained hexapod robot (Weaver) operated in outdoor terrain. This includes a detailed description of the technical background of each subsystem of the hybrid control architecture as well as results from experiments on the multi-terrain testbed and in the field.

In addition, the sensing and adaptation approaches described in this paper exploit the unique properties of a robot that has legs instead of wheels by adapting the virtual stiffness of the leg, stride frequency and stride height. The terrain estimation is designed to describe the terrain by the two parameters roughness and step height. This minimal representation of the terrain reduces the complexity of the environment and enables Weaver to feed back this information into its control system.

Our main contribution is the adaptation based on exteroceptive, proprioceptive sensing and a combination of both sensing methods. Proprioceptive sensing uses the unique kinematic properties of Weaver by extracting terrain features from the interaction with the environment. Moreover, the combination of exteroceptive and proprioceptive sensing is robust against situations where the robot is blind, i.e., where the robot is not able to accurately generate a representation of the terrain by using its exteroceptive sensing capabilities. Terrain perception using only proprioceptive sensing is an effective method that does not require additional hardware and computational power.

Future work will exploit more of the minimal terrain representation by using it for path planning and generating an overall roughness and step height map. This map is used to plan efficient and safe paths by minimizing a specific cost on the path. In addition, this global path is further used as an input to the path follower described in this work. Problems such as foothold selection and planning to enable Weaver to negotiate bigger obstacles are also candidates for future work to boost the capabilities of the robot in the field.

Acknowledgments

References

Arena, P., Fortuna, L., Frasca, M., Patané, L., and Pavone, M. (2005). Climbing obstacles via bio-inspired CNN-CPG and adaptive attitude control. In *IEEE International Symposium on Circuits and Systems (ISCAS 2005)*, pages 5214–5217. Piscataway, NJ: IEEE.

Bjelonic, M., Homberger, T., Kottege, N., Borges, P. V. K., Beckerle, P., and Chli, M. (2017). Autonomous navigation of hexapod robots with vision-based controller adaptation. In *IEEE International Conference on Robotics and Automation (ICRA)*, pages 5561–5568. Piscataway, NJ: IEEE.

Bjelonic, M., Kottege, N., and Beckerle, P. (2016). Proprioceptive control of an over-actuated hexapod robot in unstructured terrain. In *IEEE/RSJ International Conference on Intelligent Robots and Systems (IROS)*, pages 2042–2049.

Breivik, M. and Fossen, T. I. (2009). Guidance laws for autonomous underwater vehicles. In Inzartsev, A. V., editor, *Underwater Vehicles*, pages 52–76. InTech.

Chilian, A. and Hirschmüller, H. (2009). Stereo camera based navigation of mobile robots on rough terrain. In *IEEE/RSJ International Conference on Intelligent Robots and Systems (IROS)*, pages 4571–4576. Piscataway, NJ: IEEE.

Elfes, A., Steindl, R. J., Talbot, F., Kendoul, F., Sikka, P., Lowe, T., Kottege, N., Bjelonic, M., Dungavell, R., Bandyopadhyay, T., Hoerger, M., Tam, B., and Rytz, D. (2017). The multilegged autonomous explorer (MAX). In *IEEE International Conference on Robotics and Automation (ICRA)*, pages 1050–1057. Piscataway, NJ: IEEE.

Fukuoka, Y., Kimura, H., and Cohen, A. H. (2003). Adaptive dynamic walking of a quadruped robot on irregular terrain based on biological concepts. *The International Journal of Robotics Research*, 22(3-4):187–202.

Furgale, P., Rehder, J., and Siegwart, R. (2013). Unified temporal and spatial calibration for multi-sensor systems. In *IEEE/RSJ International Conference on Intelligent Robots and Systems (IROS)*, pages 1280–1286. Piscataway, NJ: IEEE.

Gehring, C., Bellicoso, C. D., Coros, S., Bloesch, M., Fankhauser, P., Hutter, M., and Siegwart, R. (2015). Dynamic trotting on slopes for quadrupedal robots. In *IEEE/RSJ International Conference on Intelligent Robots and Systems (IROS)*, pages 5129–5135. Piscataway, NJ: IEEE.

Görner, M., Wimböck, T., Baumann, A., Fuchs, M., Bahls, T., Grebenstein, M., Borst, C., Butterfass, J., and Hirzinger, G. (2008). The DLR-Crawler: A testbed for actively compliant hexapod walking based on the fingers of DLR-Hand II. In *IEEE/RSJ International Conference on Intelligent Robots and Systems (IROS)*, pages 1525–1531. Piscataway, NJ: IEEE.

Goswami, A., Thuilot, B., and Espiau, B. (1998). A study of the passive gait of a compass-like biped robot symmetry and chaos. *The International Journal of Robotics Research*, 17(12):1282–1301.

Hirose, S., Tsukagoshi, H., and Yoneda, K. (2001). Normalized energy stability margin and its contour of walking vehicles on rough terrain. In *IEEE International Conference on Robotics and Automation (ICRA)*, pages 181–186. Piscataway, NJ: IEEE.

Hodgins, J. K. and Raibert, M. (1991). Adjusting step length for rough terrain locomotion. *IEEE Transactions on Robotics and Automation*, 7(3):289–298.

Hoepflinger, M. A., Hutter, M., Gehring, C., Blösch, M., and Siegwart, R. (2013). Unsupervised identification and prediction of foothold robustness. In *IEEE International Conference on Robotics and Automation (ICRA)*, pages 3293–3298. Piscataway, NJ: IEEE.

Homberger, T., Bjelonic, M., Kottege, N., and Borges, P. V. K. (2016). Terrain-dependent motion adaptation for hexapod robots. In *International Symposium on Experimental Robotics (ISER)*, pages 92–102. Springer.

Hutter, M., Gehring, C., Jud, D., Lauber, A., Bellicoso, C. D., Tsounis, V., Hwangbo, J., Bodie, K., Fankhauser, P., Bloesch, M., Diethelm, R., Bachmann, S., Melzer, A., and Hoepflinger, M. (2016). Anymal-a highly mobile and dynamic quadrupedal robot. In *IEEE/RSJ International Conference on Intelligent Robots and Systems (IROS)*, pages 38–44. Piscataway, NJ: IEEE.

Kalakrishnan, M., Buchli, J., Pastor, P., and Schaal, S. (2009). Learning locomotion over rough terrain using terrain templates. In *IEEE/RSJ International Conference on Intelligent Robots and Systems (IROS)*, pages 167–172. Piscataway, NJ: IEEE.

Kolter, J. Z., Rodgers, M. P., and Ng, A. Y. (2008). A control architecture for quadruped locomotion over rough terrain. In *IEEE International Conference on Robotics and Automation (ICRA)*, pages 811–818. Piscataway, NJ: IEEE.

Kottege, N., Parkinson, C., Moghadam, P., Elfes, A., and Singh, S. P. (2015). Energetics-informed hexapod gait transitions across terrains. In *IEEE International Conference on Robotics and Automation (ICRA)*. Piscataway, NJ: IEEE.

Leutenegger, S., Furgale, P., Rabaud, V., Chli, M., Konolige, K., and Siegwart, R. (2013). Keyframe-based visual-inertial slam using nonlinear optimization. In *Robotics: Science and Systems (RSS)*.

Leutenegger, S., Lynen, S., Bosse, M., Siegwart, R., and Furgale, P. (2014). Keyframe-based visualinertial odometry using nonlinear optimization. *The International Journal of Robotics Research*, 34(3):314–334.

Nikolic, J., Rehder, J., Burri, M., Gohl, P., Leutenegger, S., Furgale, P. T., and Siegwart, R. (2014). A synchronized visual-inertial sensor system with fpga pre-processing for accurate real-time slam. In *IEEE International Conference on Robotics and Automation (ICRA)*, pages 431–437. Piscataway, NJ: IEEE.

Pecka, M., Zimmermann, K., Reinstein, M., and Svoboda, T. (2017). Controlling robot morphology from incomplete measurements. *IEEE Transactions on Industrial Electronics*, 64(2):1773–1782.

Perez, T. (2005). Ship motion performance. In *Ship Motion Control*, Advances in Industrial Control, pages 127–142. Springer London.

Roennau, A., Heppner, G., Nowicki, M., and Dillmann, R. (2014a). LAURON V: A versatile six-legged walking robot with advanced maneuverability. In *IEEE/ASME International Conference on Advanced Intelligent Mechatronics (AIM)*, pages 82–87. Piscataway, NJ: IEEE.

Roennau, A., Heppner, G., Nowicki, M., Zoellner, J., and Dillmann, R. (2014b). Reactive posture behaviors for stable legged locomotion over steep inclines and large obstacles. In *IEEE/RSJ International Conference on Intelligent Robots and Systems (IROS)*, pages 4888–4894. Piscataway, NJ: IEEE.

Semini, C., Barasuol, V., Goldsmith, J., Frigerio, M., Focchi, M., Gao, Y., and Caldwell, D. G. (2017). Design of the hydraulically actuated, torque-controlled quadruped robot HyQ2Max. *IEEE/ASME Transactions on Mechatranics*, 22(2):635–646.

Stejskal, M., Mrva, J., and Faigl, J. (2016). Road following with blind crawling robot. In *IEEE International Conference on Robotics and Automation (ICRA)*, pages 3612–3617. Piscataway, NJ: IEEE.

Wermelinger, M., Fankhauser, P., Diethelm, R., Krüsi, P., Siegwart, R., and Hutter, M. (2016). Navigation planning for legged robots in challenging terrain. In *IEEE/RSJ International Conference on Intelligent Robots and Systems (IROS)*, pages 1184–1189. Piscataway, NJ: IEEE.

Wettergreen, D., Pangels, H., and Bares, J. (1995). Behavior-based gait execution for the Dante II walking robot. In *IEEE/RSJ International Conference on Intelligent Robots and Systems (IROS)*, pages 274–279. Piscataway, NJ: IEEE.

Wooden, D., Malchano, M., Blankespoor, K., Howardy, A., Rizzi, A. A., and Raibert, M. (2010). Autonomous navigation for BigDog. In *IEEE International Conference on Robotics and Automation (ICRA)*, pages 4736–4741. Piscataway, NJ: IEEE.

Yoshikawa, T. (1985). Manipulability of robotic mechanisms. *The international journal of Robotics Research*, 4(2):3–9.

Table 2: Range of the adaptive parameters and constant value of the non-adaptive controller.

Adaptive parameters	Min. value	Max. value	Const. value
Virtual stiffness $(\mathrm{Nm^{-1}})$	$0.75\ 10^3$	$70.34\ 10^3$	$1.06\ 10^3$
Stride frequency (Hz)	0.6	1.1	0.6
Stride height (m)	$2.31\ 10^{-2}$	$13.18\ 10^{-2}$	$9.89\ 10^{-2}$

Table 3: Performance Criteria for the exteroceptive-adaptive set: Two sets of 15 runs each have been conducted to examine the average CoT reduction and the percentage reduction of variance for each segment of the multi-terrain testbed.

Segments of the testbed	CoT reduction in %	S_{roll} in %	S_{pitch} in %
A	65.82	81.41	87.70
B	36.93	34.86	-155.26
C	12.87	2.4	-23.00
D	27.11	-2.28	22.91
E	15.76	13.85	53.91
F	16.01	3.77	3.50

Appendices

A   Parameter Set of Weaver during Experimentation

The parameters of the path follower in Section 4.1.2 were set to $V_{x,max}/V_{y,max} = 10$, $R = 1\,\mathrm{m}$, $R_{next} = 0.5\,\mathrm{m}$, $K_{rot} = 1$ and $\alpha_{e0} = 0.6\,\mathrm{rad}$. A fourth order Runge-Kutta solver was solving the differential equation in Section 4.2.2 and the non-adaptive parameters of the impedance controller were set to $\omega_0 = c_{virt}/m_{virt} = 0.89\,\mathrm{s^{-1}}$ and $D = b_{virt}/(2\sqrt{m_{virt}c_{virt}}) = 0.7$. In the inclination controller in Section 4.2.3 the parameters were set to $k_{p,1} = k_{r,1} = 0.35$ and $k_{p,2} = k_{r,2} = 0.75$, which are explained in detail in Bjelonic et al. (2016). In Section 4.3.1 the weighting parameters of the exteroceptive terrain perception were set $a_{e,1} = 0.75\,\mathrm{m^{-1}}$, $a_{e,2} = 0.05\,\mathrm{rad^{-1}}$, $a_{e,3} = 0.05\,\mathrm{rad^{-1}}$, $a_{e,4} = 0.05\,\mathrm{m^{-2}}$, $a_{e,5} = 0.1$, $a_{e,6} = 0.8\,\mathrm{m^{-1}}$, $a_{e,7} = 0.2$ and the maximum values of the normalized terrain characteristics were set to $r_{e,max} = 1$ and $h_{a,max} = 1$. Similar, the parameter set of the proprioceptive terrain perception in Section 4.3.2 was given by $a_{p,1} = 91.0\,\mathrm{m^{-1}}$, $a_{p,2} = 0.0625\,\mathrm{rad^{-1}}$, $a_{p,3} = 0.0625\,\mathrm{rad^{-1}}$, $a_{p,4} = 6.25\,\mathrm{rad^{-2}s^2}$, $a_{p,5} = 6.25\,\mathrm{rad^{-2}s^2}$, $r_{p,max} = 1.25$. The proprioceptive step height estimation was defined with the following parameter set: $\sigma_f = 100\,\mathrm{N}$, $\Delta t = 2\,\mathrm{s}$, $h_{add} = 0.0165\,\mathrm{m}$, $h_{max} = 0.1318\,\mathrm{m}$. The range of the adaptive parameters in Section 4.3.3 and the constant values of the non-adaptive approach are summarized in Table 2. The roughness threshold σ_r of the roughness error $|r_e - r_p|$ in (19a) is set to 0.5.

B   Percentage Reduction of Variance and CoT Reduction

Table 3 and 4 show the performance evaluation of the exteroceptive- and proprioceptive-adaptive set with respect to the non-adaptive set. The percentage reduction of variance (24) in Table 3 and 4 is calculated as the mean of the 15 runs of each set.

Table 4: Performance Criteria for the proprioceptive-adaptive set: Two sets of 15 runs each have been conducted to examine the average CoT reduction and the percentage reduction of variance for each segment of the multi-terrain testbed.

Segments of the testbed	CoT reduction in %	S_{roll} in %	S_{pitch} in %
A	47.03	31.17	86.87
B	3.82	-34.79	-92.48
C	-41.11	-33.56	-7.47
D	-23.45	-17.63	4.94
E	-60.46	8.01	-28.56
F	-32.49	-15.51	-19.70